Augmentation of surface plasmon-enhanced second harmonic generation from Au nanoprisms on SiO2/Si : interference contribution

Research Article Vol. 30, No. 12 / 6 Jun 2022 / Optics Express 22161
Optics EXPRESS

Augmentation of surface plasmon-enhanced second harmonic generation from Au nanoprisms on SiO_2/Si: interference contribution

ATSUSHI SUGITA,[1,*] KANTA MOCHIDUKI,[1] YUHKI KATAHIRA,[1] SOON HOCK NG,[2] AND SAULIUS JUODKAZIS[2]

[1]Department of Applied Chemistry and Biochemical Engineering, Shizuoka University, 3-5-1 Johoku, Hamamatsu, Shizuoka 432-8561, Japan
[2]Optical Sciences Centre and ARC Training Centre in Surface Engineering for Advanced Materials (SEAM), School of Science, Swinburne University of Technology, Hawthorn, VIC 3122, Australia
*sugita.atsushi@shizuoka.ac.jp

Abstract: We present an augmentation of Surface Plasmon (SP)-enhanced second harmonic generation (SHG) due to interference field enhancement in Au nanoprisms (AuNPs) on SiO_2-coated Si substrates. The SiO_2 spacer contributed for the optical interference and increased the coupling efficiency of the pump light with the SP polarization as well as a decoupling efficiency of the SHG waves from nonlinear polarization. The intensity of the SP-enhanced SHG signals increased 4.5-fold with respect to the AuNPs on the bare SiO_2 substrate by setting the SiO_2 spacer layer to the appropriate thickness. The numerical analysis revealed that the optimal SHG conversion was determined by the balance between the degree of the optical interference at the fundamental and SHG wavelengths.

1. Introduction

Nonlinear plasmonics is one of the most important applications for the surface plasmon (SP) enhanced optical fields [1–4]. Irradiating metal thin films or nanoparticle with optical field creates SPs, the collective oscillation of conducting electrons. Upon creation of SPs, the amplified and confined optical fields are generated on the surfaces of films/nanoparticles. In nonlinear plasmonics, the formation of nonlinear polarization on the metal surfaces due to the SP-enhanced optical fields is the key mechanism. The nonlinear light-matter interactions involving the SP-enhanced optical fields give rise to a great variety of nonlinear wave mixing effects, such as second harmonic generation (SHG), third harmonic generation (THG), and four wave mixing (FWM), at nanoscale.

Recently, great efforts have been made in research and development of meta-surfaces [5–8]. These regularly arranged two-dimensional arrays of structured plasmonic metal nanoparticles are useful for controlling the polarization, phase and amplitude of the light field with a high degree of flexibility. Several unique and exotic optical behaviors were achieved, such as extraordinary reflection and transmission [9], imaging using a flat lens [10], optical spin-Hall effect [11] or generation of an optical vortex [12]. The novel concept of the meta-surfaces has already been transferred into nonlinear optics [13]. It allows not only conversion of light wavelengths, but control over the wavefront as well. There have been several reports about the generation of Airy beams [14], optical vortexes [15] and holographic images [16] by the wavelength-converted light from flat nonlinear meta-surfaces.

The generation of the Airy beams [17], vortex beams [18], and holographic imaging [19] have been also achieved by using nonlinear photonic crystals (NPCs) or, domain-engineered bulky nonlinear optical medium. The NPCs overwhelm the plasmonic metasurfaces in the

#460118 https://doi.org/10.1364/OE.460118
Journal © 2022 Received 4 Apr 2022; revised 20 May 2022; accepted 22 May 2022; published 3 Jun 2022

Optics EXPRESS

efficiencies of the wavelength-conversions, because of their high nonlinear susceptibilities. On the other hand, the constituent metal nanostructures can be engineered flexibly by taking advantage of the nanofabrication technique, especially electron- and photo-lithographs in the plasmonic metasurfaces.

In these days, the nonlinear operations of the all-dielectric resonators are studied vividly, and they are also promising as the building blocks of the metasurafeces [20–22]. Higher-order terms, such as electric multipole and magnetic dipole terms, are manipulated more easily in the metasurfaces based on the plasmonic nanostructures than in those based on the all-dielectric resonators. The wavefronts are more flexibly tailored with higher degree of freedom in the former than in the latter.

The efficiencies of the nonlinear wave mixing are limited by the low damage threshold of metals, short nonlinear interaction length, the ohmic loss and the low nonlinear coefficients of the metals in plasmonic metal nanostructures. It is necessary to overcome these obstacles for nonlinear plasmonic systems to become practical. Several uniquely designed metal nanostructures have been proposed for nonlinear optical applications. More efficient SHG and THG conversions were obtained from plasmonic metal nanostructures which supported magnetic dipole or Fano resonances, as compared to the conventional purely electric dipole resonances [23–25]. The strong field confinements in the space between adjacent metal nanoparticles (nanogap) were useful for further enhancing the Raman scattering cross section [26]. Similarly, dimeric metal nanoparticles separated by a few nm-gap gave one or two magnitudes higher SHG and THG conversions than the single particles [27,28]. The doubly-resonant structures, or the structures, which satisfied both the SP resonances at the fundamental and SHG wavelengths simultaneously, were also promising for boosting the efficiencies of the SHG conversions [29,30].

Breaking the centro-symmetry in nonlinear optical media is essential for second-order nonlinear optics [31]. This rule is also crucial for operation in nonlinear plasmonics. Even centrosymmetric metal nanoparticles exhibited second-order nonlinear susceptibilities because of the electric quadrupole resonances related to the electric field gradients [32,33]. However, the SHG signals obtained from them were weak. Non-centrosymmetric metal nanoparticles, such as L-shaped [34], U-shaped [23,35], T-shaped dimers [36] and cut-rings [37], exhibited much higher SHG conversion efficiencies than the centrosymmetric nanoparticles/structures.

It is promising to use a combination of the traditional SP field enhancement effects with other approaches to gain a further enhancement of nonlinear light-matter interaction at the nanoscale. In the present study, we achieve this goal by inserting a dielectric optical interference (OI) layer between the plasmonic metal nanoparticles and the substrates. It was designed for the following two reasons. First, we tried boosting the optical fields near the metal nanoparticles by combining the incident and back-reflected light in phase. The plasmon polarizations were more efficiently coupled with the constructively interfered incident lights on the OI layer than on the ordinary substrate in a single light path. Consequently, the nonlinear polarizations were created and contributed to a more intense field. Secondly, the nonlinear polarization scattered the frequency-converted light into both forward and backward propagating components. Because of the existence of the OI layer, the forward-scattering frequency-converted light back-reflected at the OI layer/substrate interface. We extracted the frequency-converted light with a high efficiency by combining the back-scattered and back-reflected (of forward-scattered) components which were in phase.

The devices consisted of the Au nanoparticles (AuNPs), SiO_2 spacer layer for the OI layer, and a Si substrate. The schematic of the structure is shown in Fig. 1(a) and will be referred to as AuNP/SiO_2/Si going forward. We benefited from a high refractive index of Si, exceeding 3.5 in the visible region [38]. Because of a large difference in the refractive indices between SiO_2 and Si, a high Fresnel reflectance is gained at their interface. The device structure is useful for improving

Optics EXPRESS

the performance of multiple nonlinear optical mixing phenomena. Here, we demonstrate the usefulness of the proposed strategy by making an examination of the SHG phenomena.

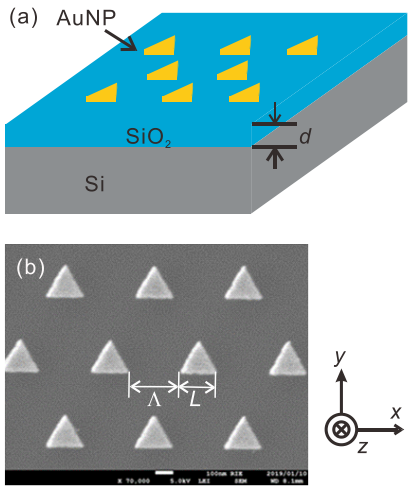

Fig. 1. (a) Schematics of AuNP/SiO_2/Si structure. (b) SEM image of AuNPs on SiO_2/Si substrate. The side length and the thickness of AuNP are $L = 170$ and $T = 30$ nm, respectively, and the edge-to-edge separations between adjacent AuNPs is Λ=300 nm. The definition of coordinate is also shown.

Our previous study reported surface enhanced Raman scattering (SERS) phenomena of the Au nanoclusters on the SiO_2/Si OI-substrate [39]. We gained approximately 14-fold enhancement of the SERS signals at the appropriate SiO_2 spacer layer thickness with respect to the Au nanoclusters on the bare SiO_2 substrate. For SERS applications, the optimal performance was obtained by just tuning the SiO_2 spacer layer thickness for the constructive interference at the pump light wavelength. This was because the pump and Raman scattering wavelengths were close to each other. The condition for the constructive interference at the Raman scattering wavelength was almost simultaneously satisfied at the same SiO_2 spacer layer thickness.

In contrast, the SHG wavelength is half the fundamental. It is unlikely that the condition for the perfectly constructive interference is satisfied simultaneously at the two wavelengths because of the wavelength dispersion of the SiO_2. We have to consider not only the degree of OI at the two wavelengths but also the balance between them for the optimal SHG conversions. It is crucial to control the interfered optical phases appropriately at the two wavelengths for the augmented SP-enhanced SHG conversion.

In the present study, the AuNP/SiO_2/Si structures were first prepared with several different SiO_2 spacer layer thicknesses. The condition for the optimal SHG conversion was determined by studying the dependence of the far-field SHG intensities on the SiO_2 spacer layer thickness. Next, the near-field intensities were calculated at the fundamental and SHG wavelengths by finite-difference time-domain (FDTD) method to address the field enhancements due to the OI at the two wavelengths. Furthermore, the far-field SHG signals was reproduced by using the field enhancement factors at these two wavelengths. Finally, we discuss formation of SP polarization on the OI-substrate, nonlinear light-matter interaction at AuNP and propagation of SHG waves into the far-field, by comparing the experimental data with numerical simulations.

Our preliminary research already suggested that it was beneficial to insert the OI layer between the AuNP and Si substrate for the additional increase in the SP-enhanced SHG conversions [40]. However, the phenomena were understood only phenomenologically, and the profound mechanism of the OI enhancements were not addressed at all. In the present study, we provide

Optics EXPRESS

clear solutions about the optimal conditions as well as the mechanism of the SHG conversions at the AuNP on the OI substrate, supported by the detailed experimental data about the dependency on the spacer layer thickness and the systematic numerical analysis based on effective nonlinear susceptibility method. Effects at the fundamental and SHG wavelengths are decoupled, which is new and significant in the present study.

2. Experimental

The AuNP/SiO_2/Si structure was prepared through two steps. First, the SiO_2 spacer layer was grown on the Si substrate by thermal oxidization method at 1000 °C. The thickness of the SiO_2 spacer layer was tuned between $d = 60$ and 400 nm by changing the annealing time. Next, the AuNPs were fabricated by an electron beam lithography method. A lift-off process was used for pattering the Au thin film on the surface of the SiO_2 spacer layer. AuNPs with equilateral triangular prism shape were prepared. A SEM image of the AuNP is shown in Fig. 1(b). The geometry of the AuNP was noncentro-symmetric, and it was suitable for the electric dipole-type second-order nonlinear optical susceptibilities. The length of each side was $L = 170$ nm and the thickness was $T = 30$ nm. The AuNPs were arrayed in a two-dimensional hexagonal lattice on the SiO_2 surface. Hence, the point symmetry of the two-dimensionally arrayed AuNPs were regarded as the C_{3v} point group. The edge-to-edge separation between two neighboring AuNPs was Λ=300 nm. The footprint of the array was a 150×150 μm square area.

The definition of the laboratory axis is also shown in Fig. 1. One of the sides of the equilateral triangle is defined as the x-axis, and the y-axis is perpendicular to it. The AuNPs were also made on bare SiO_2 substrates for comparison. It is referred to as the AuNP/SiO_2 structure. The bare SiO_2/Si structure, or the SiO_2/Si substrate without AuNPs, was also prepared to examine the OI behaviors of the substrate.

The scattering spectrum was measured for characterization of SP resonance behaviors of the samples. A white light from tungsten lamp was coupled with a step index multimode optical fiber with ϕ100 μm-diameter for shaping the beam. After propagating through a Glan-Taylor prism, the linearly polarized light was loosely focused on the sample's surfaces at normal incidence with a plano-convex lens. The spectra of the back-scattered light were measured with a multi-channel spectrometer. Unstructured Au thin film grown on the substrate was tested as reference. The white light illuminated the area and its reflection was used as reference for the scattering spectroscopy. The strong absorption of the Au prevented us from measuring the spectra at the wavelengths below 500 nm.

The pump light source for SHG spectroscopy were femtosecond optical pulses from mode-locked Ti: sapphire laser (Tsunami, Spectra Physics Inc.). The oscillation wavelength was tunable between 730 and 920 nm. The repetition rate of the optical pulses was 75 MHz, and the typical pulse energy was ~4 nJ. The polarization direction of the fundamental optical pulses was rotated with a half-wave plate. The pump beams were irradiated on the samples after loosely focusing with a plano-convex lens. The beam diameter on the sample was ϕ~100 μm. The SHG signals were measured in the back-reflection geometry. After passing a Glan-Taylor prism, they were spectrally resolved with a multi-channel spectrograph (SpectraPro SP-500, Princeton Instruments) and detected with a liquid-nitrogen cooled CCD camera (SPEC-10, Roper Scientific, Inc.). The signals were measured by changing the oscillation wavelength of the optical pulses to obtain the SHG excitation spectra.

The FDTD simulations were performed by using FullWAVE software (Rsoft Design Group, Inc.). The plane wave was launched onto the AuNP from the air side. The pulsed and monochromatic light sources were used for calculating the scattering spectra and the spatial distributions of the near-fields. The perfectly matched layer conditions were assumed in the light propagation direction, while the periodic boundary conditions were assumed in the direction perpendicular to it.

Optics EXPRESS

3. Results and discussion

3.1. SiO_2 spacer effect at the fundamental wavelength

Figure 2 shows the scattering (red solid curves) and SHG excitation spectra (blue open circles) of the AuNP/SiO_2/Si structures with different SiO_2 spacer layer thicknesses. The spectra of the AuNP/SiO_2 structure correspond to the data at d=∞ nm. The reflection spectra are also shown for the SiO_2/Si structure (green dashed) and the bare Si substrate (black dotted curves). Here, the y-polarized light was used for the measurements. The SHG signals were measured without resolving the polarization state.

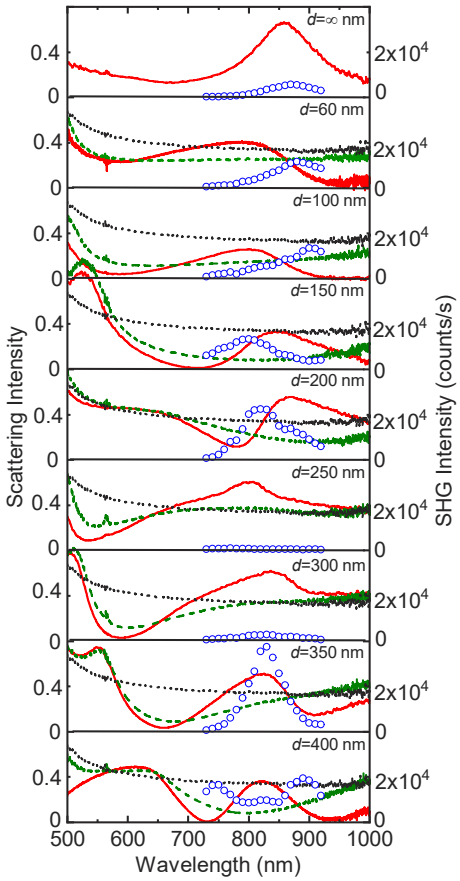

Fig. 2. Scattering (red solid curves) and SHG excitation spectra (blue open circles) of AuNP/SiO_2/Si structures with different SiO_2 spacer layer thickness d. The top figure denoted as d=∞ nm is the data of AuNP/SiO_2 structure. The green dashed and black dotted curves are the reflection spectra of SiO_2/Si structure and bare Si substrate, respectively.

First, the OI behavior of the SiO_2/Si structure compared to the reflection spectrum of the bare Si substrate is discussed. Interference fringe patterns were found in the reflection spectra and the number of the fringes increased as d became wider. Reflectivity of the SiO_2/Si structure was lower than that of the bare Si substrate in certain wavelength regions. The wavelength positions of the lower reflectivity were dependent on d. The reflectivity of the former did not exceed that of the latter at any wavelengths.

Optics EXPRESS

Constructive interference occurred, if the round-trip optical path length, $2 \cdot n_2(\lambda) \cdot d$, was equal to a half-integer multiple of the light wavelength, λ, as in Eq. (1) [41]:

$$2 \cdot d \cdot n_2(\lambda) = \left(m + \frac{1}{2}\right) \cdot \lambda \quad (m = 0,\ 1,\ 2,\ \cdots), \tag{1}$$

here, $n_2(\lambda)$ is the refractive index of the SiO_2 space layer. The π-phase shift at the SiO_2/Si interface occurs, because the light waves propagate from the SiO_2 spacer layer with lower refractive index into the Si substrate with the higher one. The reflected and incident light are in-phase at the air/SiO_2 interface, and the amplitudes of the optical fields become greater there. On the other hand, the destructive interference occurs as in Eq. (2), if the round-trip optical path length is equal to integer multiple of λ :

$$2 \cdot d \cdot n_2(\lambda) = m \cdot \lambda \quad (m = 0,\ 1,\ 2,\ \cdots). \tag{2}$$

The reflected and incident light are out-of-phase at the air/SiO_2 interface, and the amplitudes become lower there.

As will be discussed later, the AuNP exhibits the SP resonance at λ_{SP}=850 nm in the AuNP/SiO_2 structure. Paying attention to the OI-behaviors at the wavelength of excitation, the constructive interference occurs at d~141 and 425 nm, corresponding to m=0 and 1, respectively, according to Eq. (1). Here, $n_2(\lambda)$ =1.4525 at λ=850 nm was used for the estimation [42]. This condition was nearly satisfied at d = 150 and 400 nm (Fig. 2). Destructive interference occurs at d~280 nm, corresponding to m=1 according to Eq. (2) and was nearly satisfied at d = 250 and 300 nm (Fig. 2).

It is noteworthy that the degree of the OI in the SiO_2/Si structure is directly relevant to the difference in the reflectivity between the SiO_2/Si substrate and the bare Si substrate. Where destructive interference occurred, the observed reflectivity of the SiO_2/Si structures with these spacer thicknesses was much lower than that of the bare Si substrate. On the other hand, with constructive interference, the observed reflectivity was almost equal to that of the bare Si substrate. Hence, the larger the difference in the reflectivity, more destructive OI occurred and as the difference in the reflectivity approached zero, more constructive OI occurred.

3.2. Spacer effect on SHG (experimental)

Next, the linear and nonlinear optical behaviors are discussed for the AuNP/SiO_2/Si structure, along with the reference AuNP/SiO_2 structure. The scattering spectrum of the AuNP/SiO_2 structure (Fig. 2 red lines), denoted as d=∞ nm, has a peak due to the SP at λ_{SP}=850 nm. The SHG excitation spectrum has a peak at 860 nm (Fig. 2 blue open circles), which was close to the SP resonance wavelength. The SHG signals were studied for the bare SiO_2 substrates. However, there was not any measurable signals. The observed SHG signals are attributed to the nonlinear susceptibilities of the AuNPs. According to the classical Miller's rule, the nonlinear susceptibilities can be predicted by the linear susceptibilities in the electric dipole approximations [31,43]. Good agreement between the peaks of the scattering and SHG excitation spectra indicates that the SHG response of the AuNP obeys the empirical rule. Nonlinear polarizations were generated on the surface of the AuNP most efficiently at the exact SP resonance.

The SHG responses of the several plasmonic metal nanostructures were not always reproduced by the Miller's rule in previous studies [23,44,45]. It was because higher-order processes, such as the electric quadrupole and magnetic dipole terms, sometimes contributed to the nonlinear optical responses [46] but did not give significant contributions to the linear responses. Thus, the nonlinear spectra disagreed with the linear ones. In contrast, the geometry of the present equilateral triangular AuNP was obviously non-centrosymmetric, and it was suitable for electric dipole-type second-order nonlinear optics [47]. The bright electric dipole term predominantly determined the SHG conversion behaviors on the AuNPs. Accordingly, the SHG excitation spectra were in a good agreement with the scattering ones.

Optics EXPRESS

By contrast with the AuNP/SiO_2 structure, the scattering spectra of the AuNP/SiO_2/Si structures were modulated by the OI effect, and the shapes were complicated. The peak wavelength in the scattering spectrum was dependent on d, and it was not always located at 850 nm, the peak of the reference AuNP/SiO_2 structure. The SHG excitation spectra also exhibited complex behaviors probably under the influence of the OI.

The peak wavelength of the SHG excitation spectra was not in a good agreement with that of the scattering ones except for the structure with $d = 350$ nm. The SHG peak appeared at the wavelengths much longer than that of the scattering one at $d = 60$ and 100 nm, while the opposite occurred at $d = 150$ and 200 nm. In the structure with $d = 400$ nm, the SHG intensity was minimum at the 820 nm-scattering peak and instead had the two maxima at around 750 and 880 nm.

The SHG intensities also changed according to d, being much higher than the reference AuNP/SiO_2 structure at $d = 200$ and 350 nm. The peak SHG intensity at $d = 350$ nm was 4.5 times as high as that of the reference. On the other hand, it was only 0.1 at $d = 250$ and 0.2 at $d = 300$ nm, with respect to the intensities from the reference. The SiO_2 spacer layer with the appropriate thickness was helpful to increase the SP-enhanced SHG from the AuNPs.

The observed d-dependence of the SHG conversion efficiencies is explained partly in term of the OI effects at the fundamental wavelength. The SHG intensities at $d = 250$ and 300 nm were much lower than that of the AuNP/SiO_2 structure. As mentioned above, these SiO_2 layer thicknesses were close to $d = 280$ nm, the thickness which satisfied the condition for destructive interference in Eq. (2). Since the amplitudes of the optical fields were reduced by the destructive interference, the pump lights at the fundamental wavelength were coupled with SP polarizations less efficiently and the SHG conversions were reduced.

On the other hand, constructive interference in the SiO_2/Si structure did not always result in boosting the SHG conversion efficiencies. According to Eq. (1), the condition of the exact constructive interference was satisfied at $d = 140$ and 430 nm. However, the SHG intensities at $d = 150$ and 400 nm were much lower than the maximum at $d = 350$ nm in Fig. 2. The OI behavior at the fundamental wavelength alone do not explain the far-field SHG intensities from the AuNP/SiO_2/Si structure.

The SHG power conversion efficiencies were studied by measuring the average SHG power against the average pump power. Figure 3 shows the average SHG power from the AuNP/SiO_2/Si and AuNP/SiO_2 structures against the average pump power in a double logarithmic plot. The fundamental wavelength of the pump light was λ_F=850 nm. Here, the data at $d = 350$ nm is presented for the AuNP/SiO_2/Si structure. The slope of the graph is 1.90 for the AuNP/SiO_2/Si structure and 1.86 for the AuNP/SiO_2 structure indicating that the SHG conversions had a square dependence on the average pump power in both structures.

The average SHG power was $P_{SHG} = 2.0$ and 0.44 [pW] for the AuNP/SiO_2/Si and AuNP/SiO_2 structures, respectively, at $P_F = 90$ [mW]-average pump power, corresponding to 200 [MW/cm^2]-peak power. The SHG power conversion efficiencies were $\eta_{SHG} = P_{SHG}/P_F = 2.4\times10^{-11}$ for the AuNP/SiO_2/Si and 0.53×10^{-11} for the AuNP/SiO_2 structures. η_{SHG} of the AuNP/SiO_2/Si structure with $d = 350$ nm was 4.5 times as high as that of the AuNP/SiO_2 structure. Previous studies had reported that the SHG power conversion efficiencies were on the order of 10^{-11} for standard plasmonic Au nanostructures that were singly resonant with the fundamental wavelength, including split-ring resonators, and nanohole arrays [48–50]. They were much higher, when they were doubly resonant with both the fundamental and SHG wavelengths simultaneously [29,30]. H. Aouani et al. recorded the SHG power conversion efficiencies on the order of 10^{-9} in the scheme [30]. SHG power conversion efficiencies of the present AuNP/SiO_2/Si structure was on the same order of magnitude as the previous studies on the standard single resonance [29].

The polarization characteristics of the SHG signals were studied for the AuNP/SiO_2/Si ($d = 350$ nm) and AuNP/SiO_2 structures with Figs. 4(a) and (b) showing the polarization resolved

Optics EXPRESS

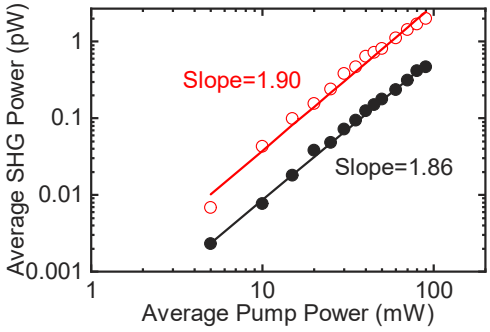

Fig. 3. Average SHG power against average pump power in double logarithmic plot for AuNP/SiO_2/Si with $d = 350$ nm (open circles) and AuNP/SiO_2 structures (filled circles). The solid lines are fit to the power function.

SHG signals for each. The measurements were performed using x- and y-polarized pump lights. There are two lobes at 0 and 180° on both x- and y-polarized pump light for the AuNP/SiO_2/Si structure. That is, the x- and y-polarized pump light at λ_F was converted into y-polarized SHG wave at $\lambda_{SHG} = \lambda_F/2$. The two lobe patterns along the y-axis were also observed from the AuNP/SiO_2 structures for both pump light polarization orientations. The AuNP converted the y-polarized SHG signals under the irradiation of the x- and y-polarized pumps, irrespective of the existence of the SiO_2 spacer layer. Hence, the OI effects in the SiO_2 spacer layer did not have any substantial influence on the nonlinear wave mixing behaviors on the AuNPs at nanoscale, except for the conversion efficiencies.

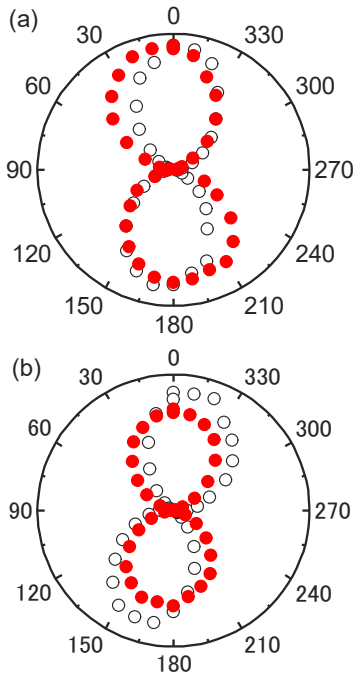

Fig. 4. Polarization-resolved SHG signals for (a) AuNP/SiO_2/Si structure with $d = 350$ nm and (b) AuNP/SiO_2 structure. Filled red and open black circles are the data against x- and y-polarized pump lights.

Optics EXPRESS

The observed polarization characteristic of the SHG signals are explained phenomenologically by using nonlinear response tensor (NRT) formalism from previous work [47]. The nonlinear susceptibility formalism for the traditional nonlinear optics makes a direct correlation between the input optical field and the nonlinear polarization. In contrast, the NRT formalism makes a direct correlation between the input and output optical fields. In general, NRT formalism is used for expressing the nonlinear optical behaviors related not only to the electric dipole terms, but also to the electric multipole and the magnetic dipole ones. They do not necessarily obey the selection rules for traditional nonlinear optics. However, the electric dipole-type selection rule is applicable to the case for the present non-centrosymmetric equilateral triangular prism-shaped AuNPs, since the electric dipole excitation and SHG emissions played a predominant rule in the nonlinear optical responses [47].

When the pump lights propagate along the z-axis, the conversions of the optical fields oscillating within the x-y plane are described with the six tensor components, that is, A_{xxx}, A_{xyy}, A_{xxy}, A_{yxx}, A_{yxy}, and A_{yyy}. The symmetry of the present system is regarded as C_{3v} point group and it is characterized with a mirror plane which includes a three-fold rotation axis [51]. Under the restriction imposed by the point symmetry of the system, only one independent tensor component A_{yxx}(=-A_{yyy} = 1/2A_{xyx}) is associated with the SHG conversion. Thereby, the y-polarized pump lights were converted into y-polarized SHG waves through A_{yyy} tensor component, while the x-polarized pump lights were converted into y-polarized SHG waves through A_{yxx} tensor component. The observed polarization behavior met the demand imposed by the point symmetry of the system.

3.3. Spacer effect on SHG (modeling)

SHG conversion behaviors of the metal nanoparticles are modeled by the nonlinear effective susceptibility method in Eq. (3) in details [45,52,53]:

$$\tilde{E}(\lambda_{SHG}) \propto \int_S \chi_{surf,\perp\perp\perp}(\lambda_F) \cdot E_\perp^2(\lambda_F) \cdot E_\perp(\lambda_{SHG}) \cdot dS \tag{3}$$

This method is based on Lorentz's reciprocity and makes a direct link between the far-field SHG waves $\tilde{E}(\lambda_{SHG})$ and the near fields created on the surface of the Au. The parameters $E_\perp(\lambda_F)$ and $E_\perp(\lambda_{SHG})$ correspond to the near fields created by fundamental waves from the pump light source and those driven by a plane wave propagating at the SHG wavelength from the detector, respectively. The $\chi_{surf,\perp\perp\perp}(\lambda_F)$ is the local surface nonlinear susceptibility tensor component of Au, where $\perp$ denotes the component normal to the surface. The tensor components $\chi_{surf,\perp//\,//}(\lambda_F)$ and $\chi_{surf,//\perp//}(\lambda_F)$, where // denotes the component in plane to the surface, are also allowed from the requirement of the point symmetry [31]. The previous study demonstrated that the component $\chi_{surf,\perp\perp\perp}(\lambda_F)$ was much larger than $\chi_{surf,\perp//\,//}(\lambda_F)$ and $\chi_{surf,//\perp//}(\lambda_F)$[54,55]. For the sake of simplicity, only the component $\chi_{surf,\perp\perp\perp}(\lambda_F)$ was considered.

According to electrodynamics, $\chi_{surf,\perp\perp\perp}(\lambda_F)$ is described explicitly by using the permittivity of vacuum ε_0, the dielectric function of Au $\varepsilon(\lambda_F) = \varepsilon_r(\varepsilon_F) + i \cdot \varepsilon_i(\varepsilon_F)$, the electron mass m, the charge of the electron e, and the velocity of light c as Eq. (4) [56,57]:

$$\chi_{surf,\perp\perp\perp}(\lambda_F) = \frac{1}{16\pi^2}[\varepsilon_r(\lambda_F) - 1] \cdot \frac{e \cdot \varepsilon_0 \cdot \lambda_F^2}{m \cdot c^2 \cdot \varepsilon(\lambda_F)^2}. \tag{4}$$

Both of them oscillate normal to the surface of the AuNP. The near fields are chosen just outside the surface of Au. In the integral of Eq. (3), the term $\chi_{surf,\perp\perp\perp}(\lambda_F) \cdot E_\perp^2(\lambda_F)$ defines intensities of the local SHG polarization sources, while the term $E_\perp(\lambda_{SHG})$ presents the decoupling efficiency of the SHG waves from the AuNP into the far-field. The integration is performed over the surface S of the AuNP.

Optics EXPRESS

The spatial electric field distributions for the *y*-polarized light were calculated with the FDTD method for AuNP/SiO_2/Si and AuNP/SiO_2 structures at the fundamental and SHG wavelengths, λ_F=850 and λ_{SHG}=425 nm, respectively (Fig. 5). The distributions are cross-sectional view in the *x*-*y* plane at a location 5 nm below the bottom surface of the AuNP and the data at $d = 150$ and 350 nm are shown for the AuNP/SiO_2/Si structure. The view in the *y*-*z* plane at $x = 0$ nm is also shown in logarithmic scale.

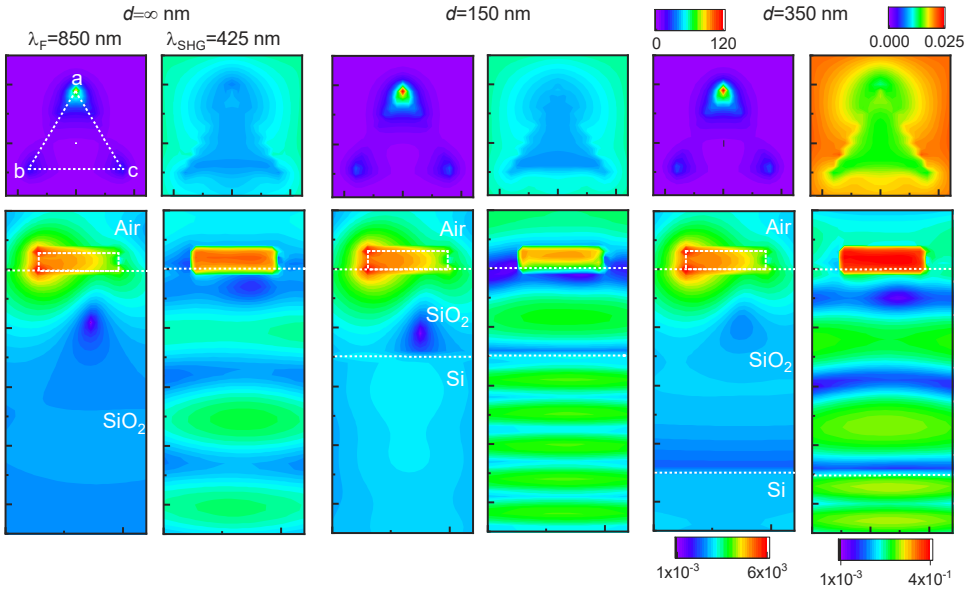

Fig. 5. Simulated field distributions of AuNP/SiO_2/Si structures at fundamental (left) and SHG wavelengths (right). The data of d=∞, 150, and 350 nm, are presented. The top graphs are the cross-sectional views in *x*-*y* plane in linear scale and the bottom ones are the views in the *y*-*z* plane in the logarithmic scale.

In the AuNP/SiO_2 structure, corresponding to d=∞ nm, the spatial field distribution ($E_\perp(\lambda_F)$) was concentrated near the three apexes of the AuNP at λ_F=825 nm shown in the Fig. 5. The intensity around the apex *a* was approximately 4 times as high as those near *b* and *c*. The distribution pattern was associated with a pair of the SP polarizations that were created between the apexes *a* and *b* and between *a* and *c*. The intensities of the two polarizations were equal to each other, and they oscillated in-phase. The nonlinear polarization sources for the SHG waves were predominantly created near the three apexes. Especially, the intensities near the apex *a* was the strongest among them. On contrast, the field distribution near the AuNP ($E_\perp(\lambda_{SHG})$) was lower than those of the surrounding region at λ_{SHG}=425 nm. It was because of the absorption loss due to the interband transition from 5d to 6sp levels [58,59]. The far-field SHG signals were attributed to the components, which were generated near the apexes and escaped from the reabsorptions in the AuNP.

As denoted in Eq. (3), the intensities of the SHG polarization sources ($\chi_{surf,\perp\perp\perp}(\lambda_F) \cdot E_\perp^2(\lambda_F)$) were proportional to the squared intensities of the local fields, and the directions were perpendicular to the Au surfaces. In the present experimental configuration, the pump lights propagated along the *z*-axis direction, or in the direction perpendicular to the *x*-*y* plane. Hence, they were created by the near fields oscillating within the *x*-*y* plane on the three side surfaces of the AuNPs.

The field distribution at the fundamental wavelength ($E_\perp(\lambda_F)$) was symmetric with respect to the *y*-*z* plane at $x = 0$ and the distribution of the SHG polarization source ($\chi_{surf,\perp\perp\perp}(\lambda_F) \cdot E_\perp^2(\lambda_F)$) must be mirror-symmetric with respect to it. The near field distribution at the SHG wavelength

Optics EXPRESS

($E_{\perp}(\lambda_{SHG})$) was also symmetric to the y-z plane at $x = 0$. The integrand $\chi_{surf,\perp\perp\perp}(\lambda_F) \cdot E_{\perp}^2(\lambda_F)$ in Eq. (3) must be distributed mirror-symmetrically with respect to the same plane. Consequently, the x-polarized far-field SHG components created on the side a-b cancelled out with those created on the side a-c. Only the y-polarized components propagated into the far-field. The numerical prediction was supported by the experimental observation of the y-polarized far-field SHG signals.

The AuNP/SiO_2/Si structures had response similar to those of the AuNP/SiO_2 structure, independent of the SiO_2 spacer layer thickness, both at λ_F and λ_{SHG}, except for the absolute strengths. The observations indicated that the OI effects due to the SiO_2 spacer layer gave significant influences on the coupling efficiencies of the fundamental lights with the SP polarizations and the decoupling efficiencies of them into far-field SHG waves. On the other hand, it did not make any essential influences on the coupling behaviors between them.

The spatial electric field distributions at $d = 350$ nm were much higher than those of the AuNP/SiO_2 structure both at λ_F and λ_{SHG}. The influence of the constructive OI effects at λ_{SHG} are visible in the y-z cross sectional view of the electric fields. The field intensities around the AuNPs was higher at $d = 150$ nm than those at d=∞ nm, because the reflected and incident electric fields were superimposed in-phase there. Both the coupling efficiencies from the fundamental lights with the SPs and the decoupling efficiencies of the SHG waves from the nonlinear polarization sources were higher in the former than in the latter. This was the reason why the AuNP/SiO_2/Si structure at $d = 350$ nm generated higher SHG signals than the reference AuNP/SiO_2 structure.

On the other hand, the electric field intensities at $d = 150$ nm were almost as high as those at $d = 350$ nm at the fundamental wavelength in the x-y cross-sectional view. The former was much lower than the latter at the SHG wavelength. The fundamental light was coupled efficiently with the SPs, and accordingly the near-field SHG polarization sources were also created with high efficiency. However, the SHG waves were decoupled from the nonlinear polarization sources less efficiently because of the destructive interference at the SHG wavelength. In the y-z cross sectional view, the field intensities around the AuNPs were lower at $d = 150$ nm than at d= ∞ nm. The reflected and incident electric fields were superimposed out-of-phase.

As presented in Fig. 3, the experimentally observed SHG intensities at $d = 150$ nm was only 0.2 of those of the AuNP/SiO_2 structure. The destructive interferences prevented from the efficient decoupling of the SHG waves into the far-fields at $d = 150$ nm. These results indicated that the OI effects not only at the fundamental but also at the SHG wavelengths determined the intensity of the far-field SHG signals.

The calculations were performed for the AuNP/SiO_2/Si structures with other SiO_2 spacer layer thicknesses. Figure 6(a) shows the calculated scattering spectra along with the experimental data showing good agreement between the two. The photonic mode such as surface lattice resonances could occur in the present system, because of the multilayer structure and the periodic array of the plasmonic AuNP. It may provide another opportunity of boosting the SHG conversions [60]. However, the spectral shape was reproduced well by the numerical model that took account of the OI and localized SP effects. Hence, the new modes were not formed there.

The calculations were also done to obtain the near-fields in the vicinity of the AuNP at the fundamental and SHG wavelengths (Fig. 6(b)). Here, the spectra were monitored in the 10 nm-square area 5 nm below the apex a of the bottom surface of the AuNP. The field intensities were much stronger there than in the other areas. The spectra were presented after normalizing by using the spectral peak intensity of the AuNP/SiO_2 structure at λ_F =850 and λ_{SHG}=425 nm. Furthermore, the far-field SHG spectra were studied numerically, and they were presented along with the experimental result in Fig. 6(c). The local surface nonlinear susceptibility tensor component $\chi_{surf,\perp\perp\perp}(\lambda_F)$ in Eq. (4) was estimated by using the data of $\varepsilon_r(\lambda_F)$ in the literature [50]. The far-field SHG signals were predominantly attributed to the nonlinear polarization sources created near apex a of the AuNP. Here, the spectra were calculated by using the data at

Optics EXPRESS

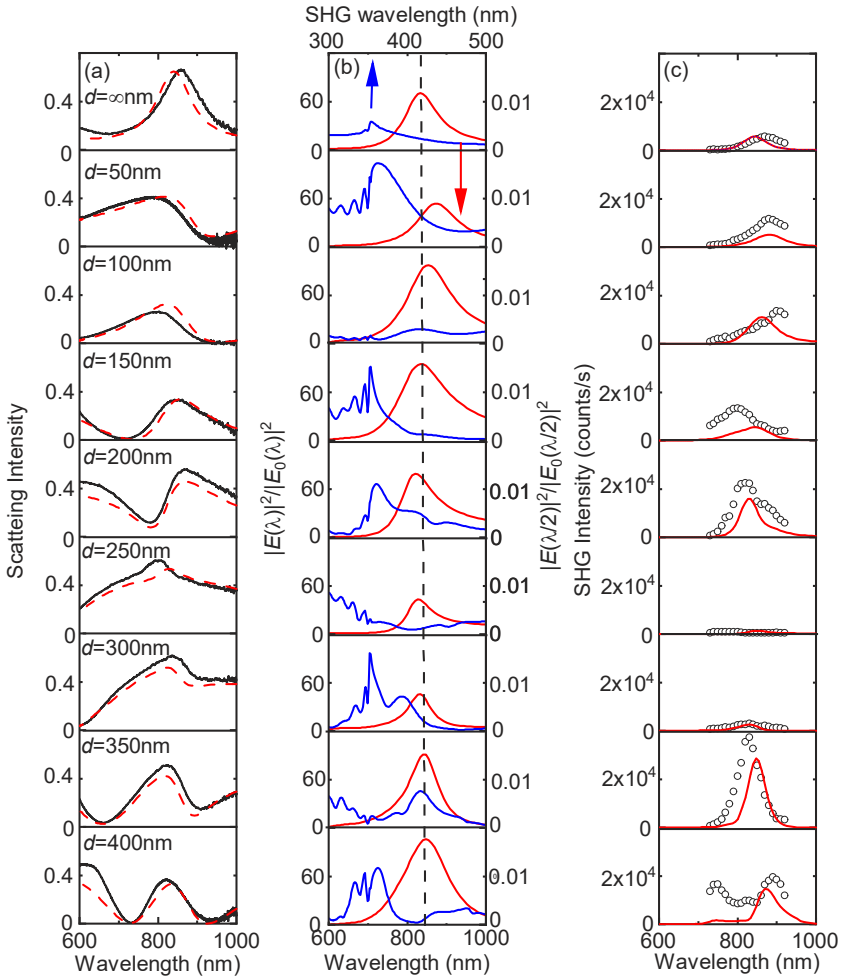

Fig. 6. (a) Experimental (black solid) and numerical far-field scattering spectra (red dashed curves) of AuNP/SiO_2/Si structures with different SiO_2 spacer layer thickness d. (b) Numerical near-field spectra at AuNP at fundamental (red solid) and SHG wavelengths (blue solid curve). The dashed line denotes the SP peak of AuNP/SiO_2 structure, corresponding to d=∞nm. (c) Experimental (black open circles) and numerical far-field SHG excitation spectra (red solid curves).

the representative point in place of performing the integration over the surface of the AuNP in Eq. (3).

The near-field spectrum had the peak at ~850 nm in the fundamental wavelength region, independent of d. In contrast, it was highly dependent on d in the SHG wavelength region and the complicated spectral behaviors of the near fields in the region significantly influenced the intensity and shape of the far-field SHG signals. In Fig. 6(c), the calculated far-field SHG spectra reproduced the experimental data in the following respects. First, the far-field SHG peak appeared in the wavelengths much longer than the peak of the SP resonance of λ_{SP}~850 nm at d = 100, 150, and 400 nm, while it appeared in the wavelengths much shorter than it at d = 200 and 350 nm. Second, the far-field SHG intensities were much lower than that of the AuNP/SiO_2 structure at d = 250 and 300 nm. Third, the spectral shape with the two peaks was reproduced at d = 400 nm. Finally, the SHG intensity was the highest at d = 350 nm among the series of the spectra.

Optics EXPRESS

The experimental and calculated far-field SHG intensities are also plotted against d at λ_F = 850 nm in Fig. 7(a). The numerical curve is in good agreement with the experimental data and reproduce the oscillating behaviors of the far-field SHG signals against d well. There are three peaks in the region from d = 0 - 400 nm with different intensities. The SHG intensity is the highest at d = 360 nm, and it is 4.2 times as high as that from the AuNP/SiO_2.

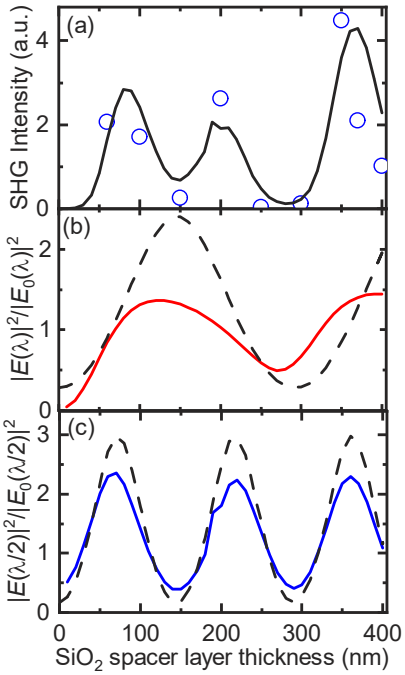

Fig. 7. (a) Experimental (open circles) and simulated SHG intensities (solid curve) against SiO_2 spacer layer thickness. Simulated field enhancements against SiO_2 spacer layer thickness at (b) fundamental and (c) SHG wavelengths. Dashed curves are the field enhancement factor due to optical interference calculated with Eq. (4).

3.4. *Enhancement factor of SHG*

The calculated near-field intensities are plotted against d at λ_F and λ_{SHG} in Fig. 7(b) and (c), respectively. The field enhancement factor due to the OI effect, EF_{OI}, was also calculated for the bare SiO_2/Si structure for the purpose of the reference, and they are shown in the figure. In the calculation of EF_{OI}, the electric field intensities were obtained by adding the amplitude of the reflected light to that of the incident one on the side of the air at the air/SiO_2 interface. The data was normalized by using the data of the bare SiO_2 substrate.

EF_{OI} is expressed explicitly by using a Fresnel reflection coefficient of the flat three-layer air/SiO_2/Si structure, $r_{123}(\lambda, d)$, as in Eq. (5) [41]:

$$EF_{OI}(\lambda, d) = \left| \frac{1 - r_{123}(r, d)}{1 - r_{123}(r, 0)} \right| \tag{5}$$

The parameter $r_{123}(\lambda, d)$ is given by

$$r_{123}(\lambda, d) = \frac{r_{12}(\lambda) + r_{23}(\lambda) \cdot \exp[-2i\delta_2(\lambda, d)]}{1 + r_{12}(\lambda) \cdot r_{23}(\lambda) \cdot \exp[-2i\delta_2(\lambda, d)]} \tag{6}$$

Optics EXPRESS

with the phase term due to the propagation inside the SiO_2 spacer layer, $\delta_2(\lambda, d) = \frac{2\pi \cdot n_2(\kappa) \cdot d}{\lambda}$. The Fresnel reflection coefficients at air/SiO_2 and SiO_2/Si interfaces at the normal incidence are given as

$$r_{12}(\lambda) = \frac{n_2(\lambda) - n_1(\lambda)}{n_2(\lambda) + n_1(\lambda)} \tag{7}$$

$$r_{23}(\lambda) = \frac{n_3(\lambda) - n_2(\lambda)}{n_3(\lambda) + n_2(\lambda)}. \tag{8}$$

Here, $n_1(\lambda)$, $n_2(\lambda)$ and $n_3(\lambda)$ are the refractive indexes of air, SiO_2, and Si, respectively; for calculations, the data were used from Refs. [38,42].

The near-field intensity had two peaks at $d = 140$ and 360 nm in the fundamental wavelength region. The intensity also took almost the maximum at $d = 360$ nm at the SHG wavelength. Hence, the far-field SHG intensity was the highest at this thickness. On the other hand, the intensity at $d = 140$ nm was almost minimum in the SHG wavelength region because of destructive OI. Consequently, even though the SP polarizations were coupled efficiently with the fundamental light, the far-field SHG intensities were low.

It should be noted that the maximum near-field intensity of the AuNP/SiO_2/Si structure was much lower than that of EF_{OI} in Fig. 7(b) and (c). The tendency was more pronounced at the fundamental than at the SHG wavelengths with the former about 60% of the latter at the fundamental and 80% at the SHG wavelengths. It was probably because of the reduced visibility of the interference due to the existence of the AuNPs on the substrates.

AuNPs worked as a scatterer and they deformed the wavefronts of the incident and reflected lights. In the present experimental conditions, the AuNPs covered only 7% of the substrate surface. However, they disrupted the wavefronts non-negligibly under the exact SP resonance conditions at the fundamental wavelength. On the other hand, the SHG wavelength was far from the SP resonance of the AuNPs. Because of the limited disruption of the wavefronts, the interference visibility was not reduced significantly. If the density of the AuNPs is sparser on the surface of the substrate, we predict a higher gain in the far-field SP-enhanced SHG signals due to the OI effect.

Recently, Xuecai Zhang et al. reported the approximately 750-fold enhancements in the SHG conversion efficiencies from the Au split ring oscillators on SiO_2 spacer layer/Au thin film/SiO_2 substrate structure [61]. Clearly, it is useful to insert the highly refractive layer between the dielectric spacer layer and the substrate for boosting the SHG conversion efficiencies. However, they presented the data only at one SiO_2 spacer thickness, and they did not seem to exhibit the clear physical role of the spacer layer on the SHG enhancements.

The present study unambiguously demonstrates the role of the OI effects in the augmented SHG conversions in plasmonic nanostructure by using the systematic experimental and numerical data on the dependency of the SiO_2 layer thickness. We also prepared the OI layer by using the simple fabrication technique of the thermal oxidation, which was another advantage of the present approach.

4. Conclusions

The present study reports surface plasmon-enhanced second harmonic generation behaviors of AuNPs grown on optical interference (OI)-substrates. Here, the OI-substrate consisted of a SiO_2/Si structure, in which the SiO_2 layer was used as the dielectric spacer and the SiO_2/Si interface worked as the high reflector. The study aimed at boosting the SHG conversion efficiencies from the AuNP by taking advantage of the field enhancements due to the OI effects in addition to the conventional SP resonances on the AuNPs. We tried increasing the SP-enhanced optical fields more by controlling the optical phases in the OI layer on the substrate and elevating the strengths of the nonlinear light-matter interactions at the nanoscale. Our experimental results

Optics EXPRESS

demonstrated that the intensities of the SP-enhanced SHG signals increased 4.5-fold with respect to those from the standard AuNPs on a bare SiO_2 substrate at the appropriated SiO_2 spacer layer thickness. FDTD analysis revealed that the OI effects had significant influences not only on the coupling of the incident light with the SP polarizations but on the decoupling from the nonlinear polarizations into the far-field SHG waves.

The present study was performed using equilateral triangular-shaped Au nanoprisms to show the effectiveness of the optical phase controlling technique for boosting SP-enhanced SHG conversion efficiencies. The technique is useful for advanced plasmonic nanostructures reported in the previous studies. We will operate the nonlinear wave mixing more efficiently by growing them on the proposed OI substrates. The enhancement factor of the present device structure is limited by the reflectivity of the SiO_2/Si interface. By replacing it with a more reflective layer, such as metallic thin films, a further increase in nonlinear conversion efficiencies is anticipated and will be analyzed in future studies.

Disclosures. The authors declare no conflicts of interest.

Data availability. Data underlying the results presented in this paper are not publicly available at this time but may be obtained from the authors upon reasonable request.

References

1. M. Kauranen and A. V. Zayats, "Nonlinear Plasmonics," Nat. Photonics **6**(11), 737–748 (2012).
2. S. B. Hasan, F. Lederer, and C. Rockstuhl, "Nonlinear plasmonic antennas," Mater. Today **17**(10), 478–485 (2014).
3. J. Butet, P. F Brevet, and O. J. F. Martin, "Optical second harmonic generation in plasmonic nanostructures: from fundamental principles to advanced applications," ACS Nano **9**(11), 10545–10562 (2015).
4. A. Krasnok, M. Tymchenko, and A. Alù, "Nonlinear metasurfaces: a paradigm shift in nonlinear optics," Mater. Today **21**(1), 8–21 (2018).
5. H.-T. Chen, A J. Taylor, and N Yu, "A review of metasurfaces: physics and applications," Rep. Prog. Phys. **79**(7), 076401 (2016).
6. Q. He, S. Sun, S. Xiao, and L. Zhou, "High-Efficiency Metasurfaces: Principles, Realizations, and Applications," Adv. Opt. Mater. **19**(6), 1800415 (2016).
7. S. Zhang, L. Liu, S. Ren, Z. Li, Y. Zhao, Z. Yang, R. Hu, and J. Qu, "Recent advances in nonlinear optics for bio-imaging applications," Opto-Electron. Adv. **3**(10), 200003 (2020).
8. Q. Chen, L. Liang, Q. Zheng, Y. Zhang, and L. Wen, "On-chip readout plasmonic mid-IR gas sensor," Opto-Electron. Adv. **3**(7), 190040 (2020).
9. X. Ni, N. K. Emani, A. Kildishev, V. A. Boltasseva, and V. M. Shalaev, "Broadband light bending with plasmonic nanoantennas," Science **335**(6067), 427 (2012).
10. M. Khorasaninejad, W. T. Chen, R. C. Devlin, J. Oh, A. Y. Zhu, and F. Capasso, "Metalenses at visible wavelengths: Diffraction-limited focusing and subwavelength resolution imaging," Science **352**(6290), 1190–1194 (2016).
11. X. B. Yin, Z. L. Ye, J. Rho, Y. Wang, and X. Zhang, "Photonic Spin Hall Effect at metasurfaces," Science **339**(6126), 1405–1407 (2013).
12. S. Chen, Y. Cai, G. Li, S. Zhang, and K. W. Cheah, "Geometric metasurface fork gratings for vortex beam generation and manipulation," Laser Photonics Rev. **10**(2), 322–326 (2016).
13. G. Li, Z. Shuang, and T. Zentgraf, "Nonlinear Photonic Metasurfaces," Nat. Rev. Mater. **2**(5), 17010 (2017).
14. S. Zur, O. Avayu, L. Michaeli, and T. Ellenbogen, "Nonlinear beam shaping with plasmonic metasurfaces," ACS Photonics **3**(1), 117–123 (2016).
15. G. Li, S. Chen, Y. Cai, S. Zhang, and K. W. Cheah, "Third harmonic generation of optical vortices using holography based gold-fork microstructure," Adv. Opt. Mater. **2**(4), 389–393 (2014).
16. N. Yu and F. Capasso, "Flat optics with designer metasurfaces," Nat. Mater. **13**(2), 139–150 (2014).
17. T. Ellenbogen, N. Voloch-Bloch, A. Ganany-Padowicz, and A. Arie, "Nonlinear generation and manipulation of Airy beams," Nat. Photonics **3**(7), 395–398 (2009).
18. N. V. Bloch, K. Shemer, A. Shapira, R. Shiloh, I. Juwiler, and A. Arie, "Twisting Light by Nonlinear Photonic Crystal," Phys. Rev. Lett. **108**(23), 233902 (2012).
19. X. Hong, B. Yang, C. Zhang, Y. Q. Qin, and Y. Y Zhu, "Nonlinear volume holography for wave-front engineering," Phys. Rev. Lett. **113**(16), 163902 (2014).
20. M. Semmlinger, M. L. Tseng, J. Yang, M. Zhang, C. Zhang, W.-Y. Tsai, D. P. Tsai, P. Nordlander, and N. J. Halas, "Vacuum Ultraviolet Light-Generating Metasurface," Nano Lett. **18**(9), 5738–5743 (2018).
21. K.-C. Shen, Y.-T. Huang, T. L. Chung, M. L. Tseng, W.-Y. Tsai, G. Sun, and D. P. Tsai, "Giant Efficiency of Visible Second-Harmonic Light by an All-Dielectric Multiple-Quantum-Well Metasurface," Phys. Rev. Appl. **12**(6), 064056 (2019).

Optics EXPRESS

22. M. L. Tseng, M. Semmlinger, M. Zhang, C. Arndt, T.-T. Huang, J. Yang, H. Y. Kuo, V.-C. Su, M. K. Chen, C. H. Chu, B. Cerjan, D. P. Tsai, P. Nordlander, and N. J. Halas, "Vacuum ultraviolet nonlinear metalens," Sci. Adv. **8**(16), 5644 (2022).
23. M. W. Klein, C. Enkrich, M. Wegener, and S. Linden, "Second-Harmonic Generation from Magnetic Metamaterials," Science **313**(5786), 502–504 (2006).
24. K. Thyagarajan, J. Butet, and O. J. F. Martin, "Augmenting Second Harmonic Generation Using Fano Resonances in Plasmonic Systems," Nano Lett. **13**(4), 1847–1851 (2013).
25. B. Metzger, T. Schumacher, M. Hentschel, M. Lippitz, and H. Giessen, "Third Harmonic Mechanism in Complex Plasmonic Fano Structures," ACS Photonics **1**(6), 471–476 (2014).
26. K. Kneipp, H. Kneipp, I. Itzkan, R. R. Dasari, and M. S. Feld, "Ultrasensitive Chemical Analysis by Raman Spectroscopy," Chem. Rev. **99**(10), 2957–2976 (1999).
27. A. Slablab, L. Le Xuan, M. Zielinski, Y. de Wilde, V. Jacques, D. Chauvat, and J.-F. Roch, "Second-harmonic generation from coupled plasmon modes in a single dimer of gold nanospheres," Opt. Express **20**(1), 220–227 (2012).
28. M. Hentschel, T. Utikal, H. Giessen, and M. Lippitz, "Quantitative modeling of the third harmonic emission spectrum of plasmonic nanoantannas," Nano Lett. **12**(7), 3778–3782 (2012).
29. H. Aouani, M. Navarro-Cia, M. Rahmani, T. P. H. Sidiropoulos, M. Hong, R. F. Oulton, and S. A. Maier, "Multiresonant Broadband Optical Antennas As Efficient Tunable Nanosources of Second Harmonic Light," Nano Lett. **12**(9), 4997–5002 (2012).
30. M. Celebrano, X. Wu, M. Baselli, S. Großmann, P. Biagioni, A. Locatelli, C. De Angelis, G. Cerullo, R. Osellame, B. Hecht, L. Duò, F. Ciccacci, and M. Finazzi, "Mode matching in multiresonant plasmonic nanoantennas for enhanced second harmonic generation," Nat. Nanotechnol. **10**(5), 412–417 (2015).
31. R. W. Boyd, *Nonlinear optics* (Academic, 2008) pp. 1–67.
32. J. Shan, J. I. Dadap, I. Stiopkin, G. A. Reider, and T. F. Heinz, "Experimental study of optical second-harmonic scattering from spherical nanoparticles," Phys. Rev. A **73**(2), 023819 (2006).
33. I. Russier-Antoine, E. Benichou, G. Bachelier, C. Jonin, and P. F. Brevet, "Multipolar Contributions of the Second Harmonic Generation from Silver and Gold Nanoparticles," J. Phys. Chem. C **111**(26), 9044–9048 (2007).
34. H. Husu, R. Siikanen, J. Mäkitalo, J. Lehtolahti, J. Laukkanen, M. Kuittinen, and M. Kauranen, "Metamaterials with Tailored Nonlinear Optical Response," Nano Lett. **12**(2), 673–677 (2012).
35. W.-Y. Tsai, T. L. Chung, H.-H. Hsiao, J.-W. Chen, R. J. Lin, P. C. Wu, G. Sun, C.-M. Wang, H. Misawa, and D. P. Tsai, "Second harmonic light manipulation with vertical split ring resonators," Adv. Mater. **31**(7), 1806479 (2019).
36. B. K. Canfield, H. Husu, J. Laukkanen, B. Bai, M. Kuittinen, J. Turunen, and M. Kauranen, "Local Field Asymmetry Drives Second-Harmonic Generation in Noncentrosymmetric Nanodimers," Nano Lett. **7**(5), 1251–1255 (2007).
37. G. Sartorello, N. Olivier, J. Zhang, W. Yue, D. J. Gosztola, G. P. Wiederrecht, G. Wurtz, and A. V. Zayats, "Ultrafast Optical Modulation of Second- and Third-Harmonic Generation from Cut-Disk-Based Metasurfaces," ACS Photonics **3**(8), 1517–1522 (2016).
38. D. E. Aspnes and A. A. Studna, "Dielectric functions and optical parameters of Si, Ge, GaP, GaAs, GaSb, InP, InAs, and InSb from 1.5 to 6.0 eV," Phys. Rev. B **27**(2), 985–1009 (1983).
39. Y. Zheng, L. Rosa, T. Thai, S. H. Ng, S. Juodkazis, and U. Bach, "Phase controlled SERS enhancement," Sci. Rep. **9**(1), 744 (2019).
40. I. Mochizuki, M. Sugiura, H. Yogo, S. Lundgaard, J. Hu, S. H. Ng, Y. Nishijima, S. Juodkazis, and A. Sugita, "Second Harmonic Generation from Phase-Engineered Metasurfaces of Nanoprisms," Micromachines **11**(9), 848 (2020).
41. M. Born and E. Wolf, *Principles of Optics, Optics Born and Wolf* (Cambridge University, 1999) pp. 1–74.
42. I. H. Malitson, "Interspecimen comparison of the refractive index of fused silica," J. Opt. Soc. Am. **55**(10), 1205–1208 (1965).
43. R. C. Miller, "Optical second harmonic generation in piezoelectric crystals," Appl. Phys. Lett. **5**(1), 17–19 (1964).
44. I. Butet and O. J. F. Martin, "Fano resonances in the nonlinear optical response of coupled plasmonic nanostructures," Opt. Express **22**(24), 29693–29707 (2014).
45. I. O'Brien, H. Suchowski, J. Rho, A. Salandrino, B. Kante, X. Yin, and X. Zhang, "Predicting nonlinear properties of metamaterials," Nat. Mater. **14**(4), 379–383 (2015).
46. I. I. Dadap, J. Shan, and T. F. Heinz, "Theory of optical second-harmonic generation from a sphere of centrosymmetric material: small-particle limit," J. Opt. Soc. Am B **21**(7), 1328–1347 (2004).
47. B. K. Canfield, S. Kujala, K. Jefimovs, Y. Svirko, J. Turunen, and M. Kauranen, "A macroscopic formalism to describe the second-order nonlinear optical response of nanostructures," J. Opt. A: Pure Appl. Opt. **8**(4), S278–S284 (2006).
48. A. Belardini, M. C. Larciprete, M. Centini, E. Fazio, C. Sibilia, M. Bertolotti, A. Toma, D. Chiappe, and F. B. de Mongeot, "Tailored second harmonic generation from self-organized metal nano-wires arrays," Opt. Express **17**(5), 3603–3609 (2009).
49. I. W. Klein, M. Wegener, N. Feth, and S. Linden, "Experiments on second- and third-harmonic generation from magnetic metamaterials: erratum," Opt. Express **16**(11), 8055 (2008).
50. J. A. H. van Nieuwstadt, M. Sandtke, R. H. Harmsen, F. B. Segerink, J. C. Prangsma, S. Enoch, and L. Kuipers, "Strong Modification of the Nonlinear Optical Response of Metallic Subwavelength Hole Arrays," Phys. Rev. Lett. **97**(14), 146102 (2006).

Optics EXPRESS

51. I. Konishi, T. Higuchi, J. Li, J. Larsson, S. Ishii, and M. Kuwata-Gonokami, "Polarization-Controlled Circular Second-Harmonic Generation from Metal Hole Arrays with Threefold Rotational Symmetry," Phys. Rev. Lett. **112**(13), 135502 (2014).
52. S. Roke, M. Bonn, and A. V. Petukhov, "Nonlinear optical scattering: the concept of effective susceptibility," Phys. Rev. B **70**(11), 115106 (2004).
53. J. Butet and O. J. F. Martin, "Evaluation of the nonlinear response of plasmonic metasurfaces: Miller's rule, nonlinear effective susceptibility method, and full-wave computation," J. Opt. Soc. Am. B **33**(2), A8–A15 (2016).
54. F. X. Wang, F. J. Rodriguez, W. M. Albers, R. Ahorinta, J. E. Sipe, and M. Kauraunen, "Surface and bulk contributions to the second-order nonlinear optical response of a gold film," Phys. Rev. B **80**(23), 233402 (2009).
55. C. Ciracì, E. Poutrina, M. Scalora, and D. R. Simth, "Second-harmonic generation in metallic nanoparticles: Clarification of the role of the surface," Phys. Rev. B **86**(11), 115451 (2012).
56. J. E. Sipe, V. C. Y. So, M. Fukui, and G. I. Stegeman, "Analysis of second-harmonic generation at metal surfaces," Phys. Rev. B **21**(10), 4389–4402 (1980).
57. G. Bachelier, J. Butet, I. Russier-Antoine, C. Jonin, E. Benichou, and P.-F. Brevet, "Origin of optical second-harmonic generation in spherical gold nanoparticle: local surface and nonlocal bulk contributions," Phys. Rev. B **82**(23), 235403 (2010).
58. I. Guerrisi, R. Rosei, and P. Winsemius, "Splitting of the interband absorption edge in Au," Phys. Rev. B **12**(2), 557–563 (1975).
59. P. B. Johnson and R. W. Christy, "Optical constants of the noble metals," Phys. Rev. B **6**(12), 4370–4379 (1972).
60. T. Abir, M. Tal, and T. L. Ellenbogen, "Second-Harmonic Enhancement from a Nonlinear Plasmonic Metasurface Coupled to an Optical Waveguide," Nano Lett. **22**(7), 2712–2717 (2022).
61. X. Zhang, J. Deng, M. Jin, Y. Li, N. Mao, Y. Tang, X. Liu, W. Cai, Y. Wang, K. Li, Y. Liu, and G. Li, "Giant enhancement of second-harmonic generation from a nanocavity metasurface," Sci. China-Phys. Mech. Astron. **64**(9), 294215 (2021).